Termination-dependent topological surface states in nodal-loop semimetal HfP₂

Christopher Sims, M. Mofazzel Hosen, Hugo Aramberri, Cheng-Yi Huang, 33 Gyanendra Dhakal, Klauss Dimitri, 1 Firoza Kabir, Sabin Regmi, Xiaoting Zhou, Tay-Rong Chang, Sabin Lin, Dariusz Kaczorowski, Tay-Rong Chang, Sabin Regmi Nicholas Kioussis,² and Madhab Neupane ^{1,*}

¹Department of Physics, University of Central Florida, Orlando, Florida 32816, USA ²Department of Physics and Astronomy, California State University, Northridge, California 91330, USA ³Institute of Physics, Academia Sinica, Taipei 11529, Taiwan ⁴Department of Physics, National Cheng Kung University, Taipei 701, Taiwan ⁵Center for Quantum Frontiers of Research & Technology (QFort), Tainan 701, Taiwan ⁶Physics Division, National Center for Theoretical Sciences, Hsinchu, Taiwan ⁷Institute of Low Temperature and Structure Research, Polish Academy of Sciences, 50-950 Wroclaw, Poland



(Received 23 June 2019; revised manuscript received 19 March 2020; accepted 1 April 2020; published 4 May 2020)

Symmetry plays a major role in all disciplines of physics. Within the field of topological materials there is a great interest in understanding how the mechanics of crystalline and internal symmetries protect crossings between the conduction and valence bands. Additionally, exploring this direction can lead to a deeper understanding on the topological properties of crystals hosting a variety of symmetries. We report the experimental observation of topological surface states in the nodal-loop semimetal HfP2 using angle-resolved photoemission spectroscopy which is supported by our first-principles calculations. Our paper shows termination-dependent surface states in this compound. Our experimental data reveal surface states linked to three unique nodal loops confirmed by theoretical calculation to be topologically nontrivial. This paper demonstrates that transition-metal dipnictides provide a good platform to study nontrivial topological states protected by nonsymmorphic symmetry.

DOI: 10.1103/PhysRevMaterials.4.054201

I. INTRODUCTION

Topological quantum matter is a growing field where the study of symmetry is applied to materials that host exotic surface states. The discovery of topological materials protected by crystalline symmetries and internal symmetries has sparked an interest in symmetry protected topological invariants [1-7]. To date, three types of topological semimetals have been discovered: Weyl semimetals [8-11], Dirac semimetals [12,13], and nodal line semimetals [14-19]. A Dirac semimetal possesses relativistic massless Dirac fermions topologically protected by crystalline symmetry and timereversal symmetry. When either time-reversal or inversion symmetry is broken, a Dirac point may split into two Weyl points with opposite chirality, which are connected by surface Fermi arcs [10]. Interestingly, topological nodal lines formed by continuous nodal points are robust and have been classified according to the crystalline symmetry that protects these states [20,21]. The nontrivial nodal loops generate enclosed surface states which are analogous to the membrane that stretches over the open end of a drum, known as "drumhead" surface states. Crystalline-symmetry protected topological states provide useful insight for investigating topological properties in symmorphic or nonsymmorphic materials [22,23]. This motivates researchers to study complex semimetals containing transition metals [9] and multiple-compound semimetals based on a desired space group for the existence of topological states [23]. One such focus is the study of nodal-line semimetals protected by crystalline symmetries which enforce robust topological states. Therefore, it is interesting to identify novel materials exhibiting topological nodal lines, protected by crystalline symmetry, more specifically materials belonging to the nonsymmorphic space group which contain glide and/or screw symmetries [24,25].

It is believed that extremely large magnetoresistance (XMR) is linked to either topological states or electron-hole compensation. To date, there has been no clear indication of the relationship between XMR and nodal line/loop states. Recent studies show that transition-metal dipnictides prove to be excellent hosts for topologically nontrivial states [26–32]. In addition, NbAs₂ has been observed to be superconducting and topologically robust at high pressures [33]. TaSb₂ has been discovered to host XMR and a nontrivial state [34,35]. While most of the previous experiments have been based on transport measurements, recent angle-resolved photoemission spectroscopy (ARPES) studies in WP₂ and MoP₂ [36-39] revealed these transition-metal dipnictides to be type-II Weyl semimetals. In general, it has been determined that transitionmetal dipnictides are mostly topologically nontrivial and also exhibit XMR. The emergence of topological states in $TaSb_2$, $NbAs_2$, and XP_2 (X = Mo, W) motivated us to study hafnium dipnictides with ARPES to further understand how the topological states arise and how they are protected. While all of the previous works have a OsGe2-type monoclinic C121 structure, our material is a transition-metal dipnictide that crystallizes in the PbCl₂-type orthorhombic Pnma structure [40].

^{*}Corresponding author: Madhab.Neupane@ucf.edu

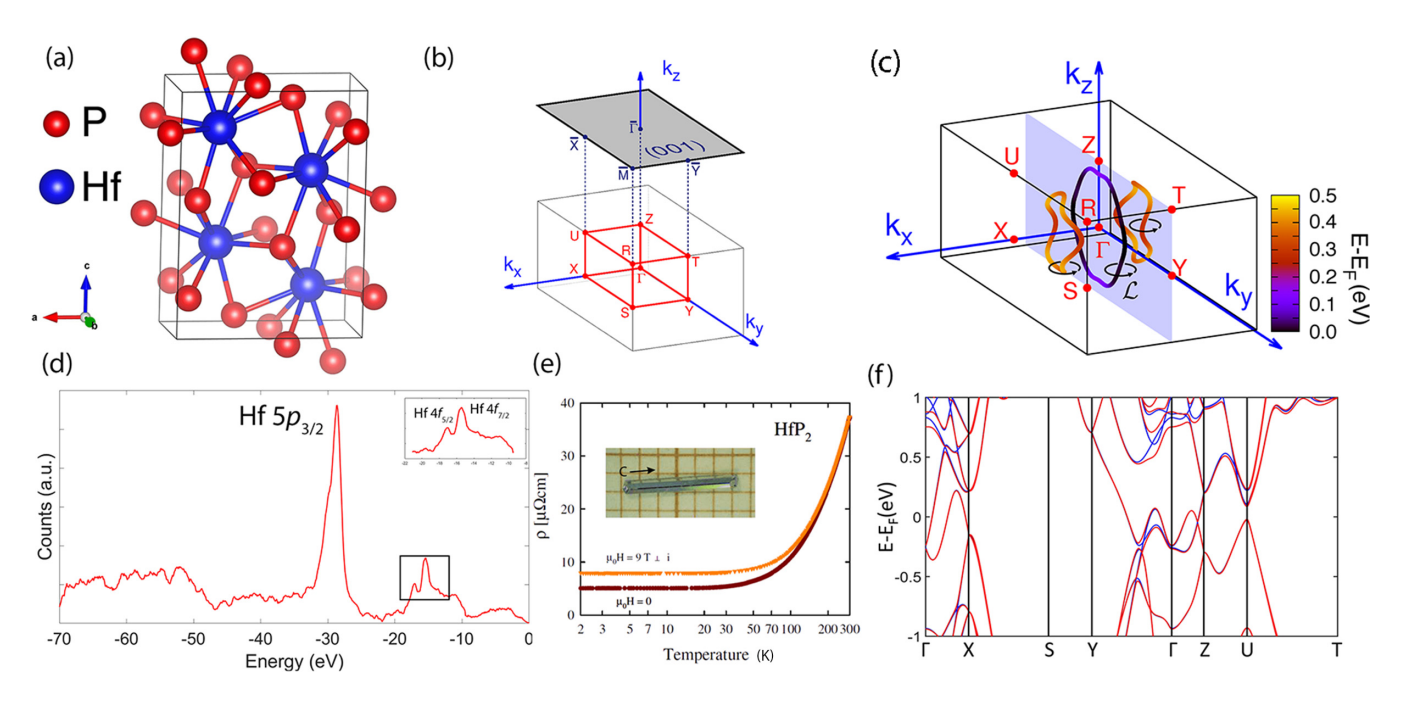


FIG. 1. Crystal structure and sample characterization. (a) The crystal structure of HfP₂ with orthorhombic space group Pnma (no. 62). (b) 3D bulk Brillouin zone of the crystal and its projection on the rectangular (001) surface. High-symmetry points are marked on the plot. (c) Nodal loops in k space where the color corresponds to the energy where the touching points occur. (d) Core-level spectroscopic measurement of HfP₂. Sharp peaks of Hf $5p_{3/2}$, Hf $4f_{5/2}$, and Hf $4f_{7/2}$ are observed. (e) Temperature dependence of the electrical resistivity of HfP₂ measured in zero magnetic field (brown) and in an external magnetic field of 9 T (orange), where the magnetic field is applied perpendicular to the current flowing along the b axis of the crystallographic unit cell. The inset shows a single crystal of HfP₂. (f) Calculated bulk bands with (red) and without (blue) SOC.

Using ARPES we report the direct observation of termination-dependent topological states in the nodal-loop semimetal HfP₂ which are confirmed by first-principles calculations. Our paper shows that the surface states are induced by two nontrivial nodal loops that exist away from the center of the Brillouin zone (BZ). Our findings provide an insight for the discovery of new topological quantum phases which emerge due to crystalline symmetries.

II. METHODS

Single crystals of HfP₂ were grown by chemical vapor transport method using iodine as a transport agent. The crystals had a form of massive rods with dimensions up to $1\times1\times8$ mm³. The chemical composition was proven by energy-dispersive x-ray analysis using a Field Electron and Ion Company scanning electron microscope equipped with an Energy Dispersive X-Ray Analysis, Genesis XM4 spectrometer. The crystal structure was examined at room temperature on a Kuma-diffraction KM4 four-circle x-ray diffractometer equipped with a CCD camera using Mo K α radiation. The experiment confirmed the orthorhombic PbCl₂-type structure (space group no. 62, *Pnma*) [40] and yielded the lattice parameters: a = 6.48 Å, b = 3.51 Å, and c = 8.69 Å.

The electrical resistivity of single-crystalline HfP_2 was measured in the temperature range of 2–300 K employing a Quantum Design Physical Property Measurement System platform. The measurements were carried out using a standard ac four-point technique with electric current flowing along the crystallographic b axis in zero magnetic field and in a field of

9 T applied perpendicular to the current. Synchrotron-based ARPES measurements were performed at the Advanced Light Source Berkeley at Beamline 10.0.1.1 equipped with a high efficiency R4000 electron analyzer. The energy resolution was better than 20 meV and the angular resolution was better than 0.2° . Samples were cleaved *in situ* and measured between 10 and 80 K in a vacuum better than 10^{-10} torr.

The electronic structure calculations were carried out within the density functional theory (DFT) framework using the VASP package [41]. We employed the Perdew-Burke-Ernzerhof [42] implementation of the generalized gradient approximation for the exchange-correlation functional. Projector augmented-wave pseudopotentials were used with an energy cutoff of 350 eV for the plane-wave basis, which was found to be sufficient to converge the total energy. The BZ was sampled with a $8 \times 15 \times 6$ k-point grid. By fully relaxing the crystal structure, the calculated lattice parameters show excellent agreement with the experimental data, the mismatch being below 0.3% for each unit-cell direction. A Wannier function-based model of the system was obtained by employing the WANNIER90 code [43], from which the electronic structure of the semi-infinite HfP2 was calculated through an iterative surface Green's-function matching technique [44] within the WANNIER tools package [45].

The spin-orbit coupling (SOC) was included self-consistently in the bulk band-structure calculations at the DFT level. Since the effect of SOC on the electronic structure was found to be rather small [see Fig. 1(f)], the SOC was not included thereafter in the computation of the WANNIER function-based model. The inclusion of SOC gaps out the

nodal loops in this system with direct and indirect band gaps of around ≈ 20 meV. Furthermore, we do not consider possible surface reconstructions on the calculations of the surface states. The theoretical Fermi level has been shifted by -200 meV hereafter, corresponding to doping effect observed in ARPES measurements. An energy disagreement between calculation and experiment is typical up to a level of around 200 meV.

III. RESULTS AND DISCUSSION

Figure 1(a) shows the crystal structure of HfP₂ where each Hf atom is coordinated by nine P atoms forming an equatorial tricapped trigonal prism. The Brillouin zone is shown in Fig. 1(b). The (001) surface of the first Brillouin zone (SFBZ) is also displayed in Fig. 1(b). Figure 1(c) shows the emergence of two sets of nodal loops: the first, centered at Γ , lies on the yz plane and is protected by glide mirror symmetry in the absence of SOC; the second set consists of two nodal loops away from the mirror plane which are protected by PT symmetry without the presence of SOC, namely, a combination of time-reversal (T) and inversion (P) symmetries.

The core-level spectra of HfP₂, shown in Fig. 1(d), are dominated by sharp peaks of Hf $5p_{3/2}$ (\approx 30 eV), Hf $4f_{5/2}$ (\approx 16 eV), and Hf $4f_{7/2}$ (\approx 14 eV), which are in line with the chemical composition of the compound. The inset shows a high resolution of the two adjacent peaks in the -20- to -10-eV energy range. The peaks appear more prominent due to a change in scale. The temperature variation of the resistivity shown in Fig. 1(e) under zero magnetic field and 9 T is typical of a metallic behavior. Figure 1(f) shows the calculated bulk band structure with (red) and without (blue) spin-orbit coupling.

We have employed two different approaches [20,46,47] to determine the Berry phase for the three nodal loops in Fig. 1(c). In the first approach, the Berry phase, W, is calculated using the Wilson loop method along an integration path, \mathcal{L} , shown in Fig. 1(c), enclosing any of the three nodal loops:

$$\mathcal{W} = \oint_{\mathcal{L}} \langle \Psi_k | i \nabla_k | \Psi_k \rangle \cdot d\ell = -\ln \det \prod_{n=0}^{N-1} P(k_n), \quad (1)$$

where $P(\mathbf{k}_n)$ is given by

$$P(\mathbf{k}_n) = \sum_{m \in \text{occ.}} |\Psi_m(\mathbf{k}_n)\rangle \langle \Psi_m(\mathbf{k}_n)|.$$
 (2)

Here, $|\Psi_m(\mathbf{k}_n)\rangle$ is the *m*th eigenvector at momentum \mathbf{k}_n on the \mathcal{L} path, $\mathbf{k}_{n+1} = \mathbf{k}_n + \delta \mathbf{k}$, $n = 0, 1, \ldots, N$, and $\mathbf{k}_0 = \mathbf{k}_N$. The system is trivial (nontrivial) if $\mathcal{W} = 0 \ (\pm \pi)$. We find that $W = \pm \pi$, indicating that the system is nontrivial.

In the second approach, we have calculated the Berry phase for the three nontrivial loops using Eq. (1) along the $k_x = -\pi/a$ to $+\pi/a$ integration path on the $k_z = 0$ plane. The Berry phase, $\mathcal{W}(k_y, k_z = 0)$, is given by

$$W(k_y, k_z = 0) = \int_{-\pi/a}^{\pi/a} \langle \Psi_k | i \partial_{k_x} | \Psi_k \rangle dk_x.$$
 (3)

Figure 2(a) shows the projection of the nodal loops centered at Γ on the yz plane where k_{y1} (k_{y2}) denote the points on the perimeter of the inner (outer) loop along the k_{y} axis.

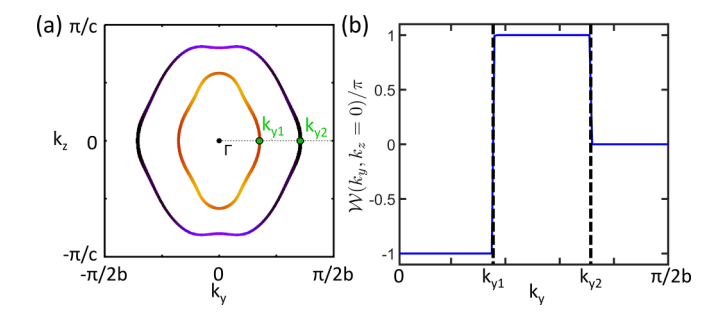


FIG. 2. (a) Projection of both nodal loops centered at Γ [see Fig. 1(c)] on the (100) plane where k_{y1} and k_{y2} denote the points on the perimeters of the inner (orange) and outer (purple) loops along the k_y axis. (b) Berry phase as a function of k_y .

In Fig. 2(b) we display the variation of $W(k_y)$ along the k_y direction. One can clearly see that the Berry phase jumps from $-\pi$ to $+\pi$ at k_{y1} and subsequently from $+\pi$ to zero at k_{y2} . A π jump of the Berry phase implies a change of number of edge modes by one. Thus, these results suggest that the number of modes changes from one in the $0 < k_y < k_{y1}$ region to three in the $k_{y1} < k_y < k_{y2}$ region and finally to two edge modes in the $k_y > k_{y2}$ region.

In this paper, we report our ARPES measurements from two kinds of samples: a fresh sample where measurements were taken right after cleaving and an aged sample which was measured after a long period of time. In order to determine the possible surface termination for each sample, we carry out systematic calculations of the projected bulk and surface states for the (001) cleavage plane for various (six nonequivalent) surface terminations. Interestingly, the calculations reveal that the surface states are extremely sensitive to the surface termination. We suggest that the P6-terminated (001) surface (see Supplemental Material [48]), shown in Fig. 3(c), yields surface states in reasonable agreement with the experimental results of the aged sample. The P6 corrugated surface consists of alternating Hf-P dimers along the [001] direction (see Supplemental Material [48]). Figures 3(a) and 3(b) show a comparison of the experimental and theoretical constant energy contours for different energy cuts. As the energy level decreases from the Fermi level, the bulk states gradually expand and the small handlelike pockets near the \overline{X} point become bigger and triangular. Figure 3(d) shows the calculated surface band structure for the P6-terminated (001) surface. The nontrivial surface states in this energy region are difficult to resolve because most of these surface states are buried in bulk states (see Supplemental Material [48]).

Figure 4 shows further comparison of the experimental and theoretical energy dispersion along the \overline{Y} - $\overline{\Gamma}$ - \overline{Y} and the \overline{M} - \overline{X} - \overline{M} high-symmetry lines. The calculated energy dispersion along \overline{Y} - $\overline{\Gamma}$ - \overline{Y} in Fig. 4(b) is in good agreement with experiment [Fig. 4(a)]. The bulk states dominate the cut while the surface states predicted in Fig. 4(b) are difficult to resolve in Fig. 4(a). The dashed lines are shown to guide the eyes on the dominant bulk states in this high-symmetry direction. The slope of the states along the \overline{M} - \overline{X} - \overline{M} direction, marked by the dashed lines in Fig. 4(c), are in good agreement with the calculations in Fig. 4(d). However, it is difficult to distinguish the nontrivial P6-terminated surface states since they

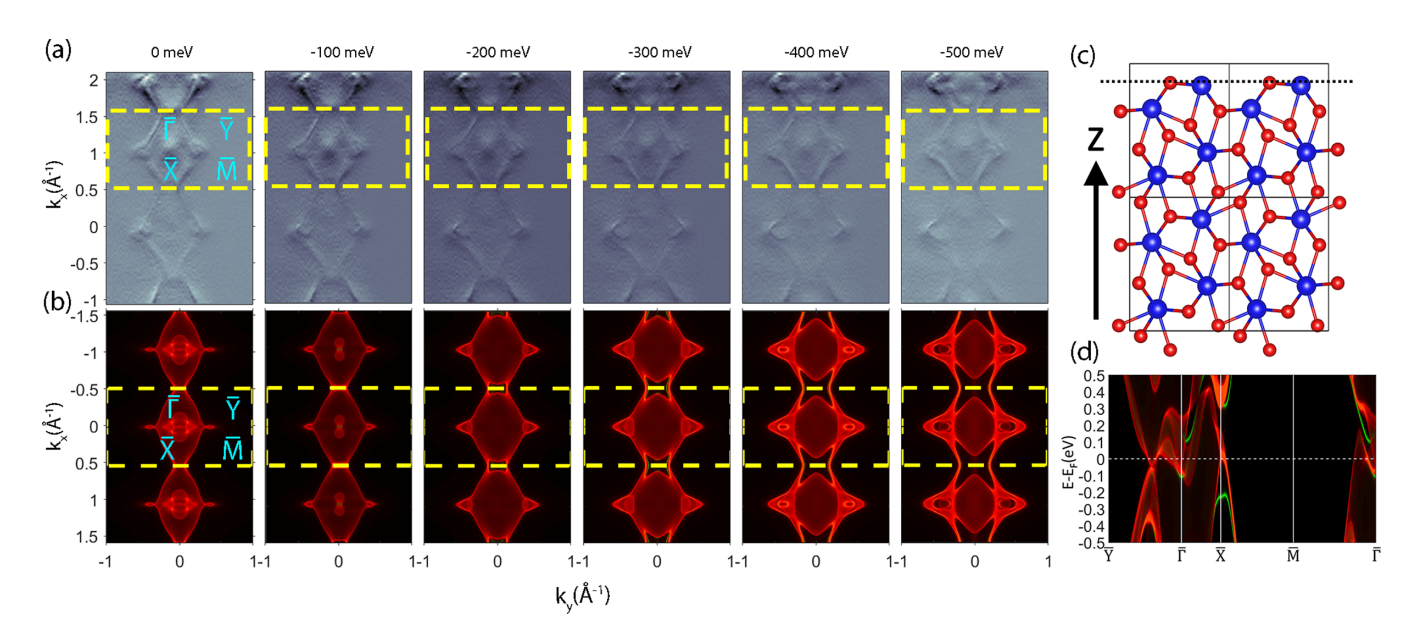


FIG. 3. Fermi surfaces and constant energy contours of the P6-terminated (001) HfP₂ surface. (a) Second derivative of experimentally measured constant energy contours and Fermi surface (photon energy hv = 57 eV) from $E - E_F = 0$ to -500 meV. (b) Calculated Fermi surface. The yellow dashed rectangles in (a) and (b) indicate the SFBZ. The size of the SFBZ along the k_y direction is three times larger than that along k_x . (c) Side view of the crystal structure of the P6-terminated (001) surface denoted with a dashed line. (d) Calculated surface band structure of the (001) P6-terminated surface. Red (green) color indicates projected bulk (surface) states.

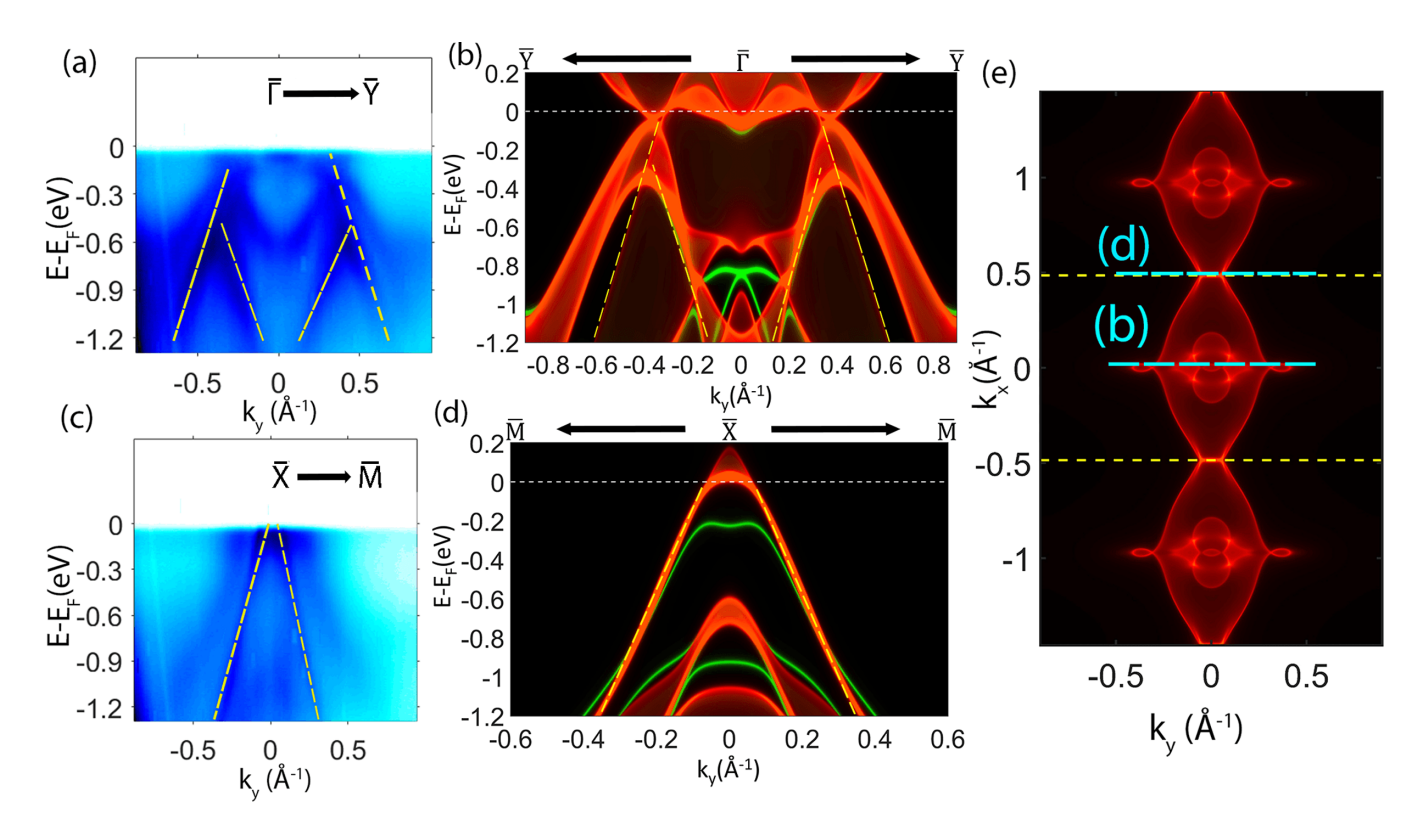


FIG. 4. High-symmetry cuts of the P6-terminated (001) surface of HfP₂. (a) Experimental constant energy cuts along the \overline{Y} - $\overline{\Gamma}$ - \overline{Y} direction with photon energy hv = 59 eV. (b) Theoretical band structure of the P6-terminated (001) surface along the \overline{Y} - $\overline{\Gamma}$ - \overline{Y} direction, where the green (red) color denotes surface states (projections of bulk bands). (c) Experimental constant energy cuts along the \overline{M} - \overline{X} - \overline{M} line with photon energy hv = 59 eV. (d) Theoretical band structure of the P6-terminated (001) surface along the \overline{M} - \overline{X} - \overline{M} direction. Yellow dashed lines are a guide to the eyes. (e) Calculated Fermi surface of the P6-terminated surface at Fermi level.

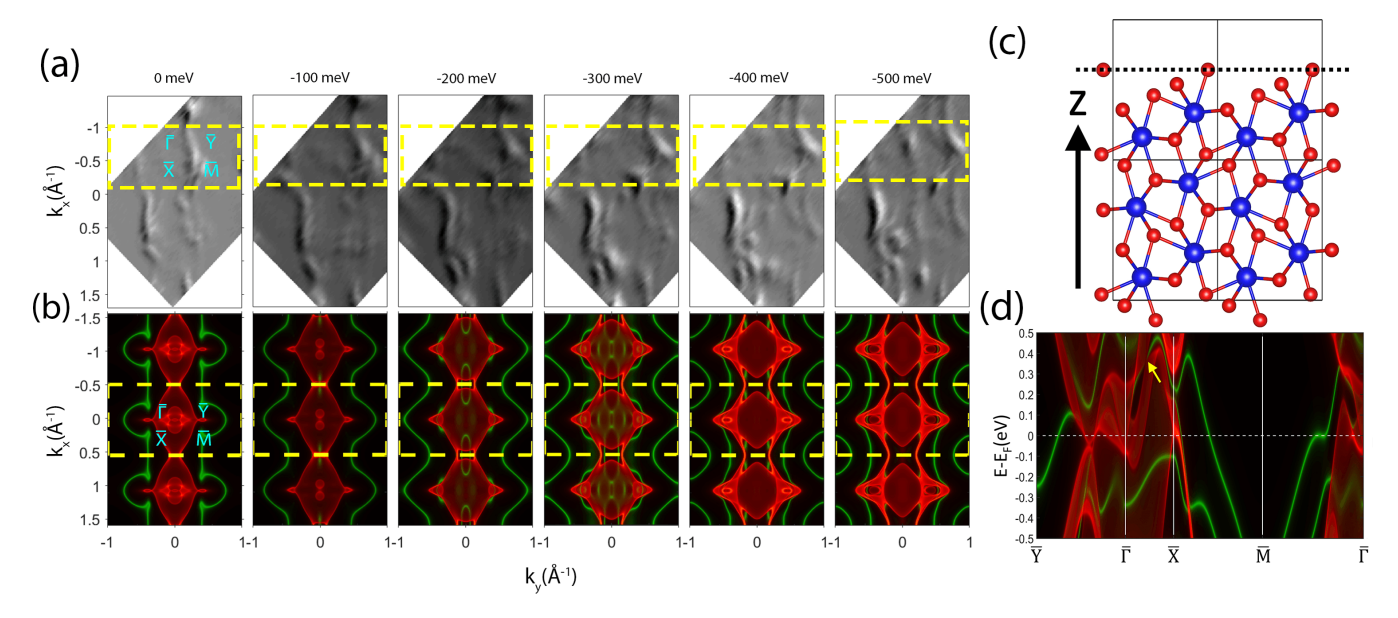


FIG. 5. Fermi surface and constant energy contours of the P7-terminated (001) surface of HfP₂. (a) Second derivative of experimentally measured constant energy contours and Fermi surface (photon energy hv = 57 eV) from $E - E_F = 0$ to -500 meV. (b) Calculated Fermi surface of the P7-terminated (001) surface. The yellow dashed rectangles indicate the SFBZ. (c) Crystal structure of the (001) P7-terminated surface indicated by the dashed line. (d) Calculated surface band structure for the P7-terminated surface. The bulk (surface) states are denoted by red (green) and the yellow arrow indicates a nontrivial crossing point from which the nontrivial surface states emerge.

are embedded in the bulk states. When we conduct photon energy dependent measurements, we see that the location of the parabolic bulk band dispersion changes with photon energy. Therefore, at this photon energy (hv = 59 eV) we see both the topological surface state and the bulk state at a photon energy that sets k_z away from the plane that we have selected for the calculations. As we tune the photon energy, we see this bulk state begins to merge with the surface state that matches the band dispersion seen in calculations in Fig. 4(d) (see Supplemental Material [48]).

In order to further understand the nontrivial surface states, we have systematically investigated various samples which are measured with different times of exposure after cleavage. The results of the ARPES measurements in a freshly cleaved sample are shown in Fig. 5, where we see the emergence of two stripelike Fermi surfaces along the k_x direction which move apart from the zone center as the binding energy decreases from the Fermi level to -500 meV. This feature is absent in the theoretical band structure of the P6-terminated (001) surface [Fig. 3(b)], which implies a different surface termination. We believe that the P7-terminated surface requires lower cleavage energy and can be easily formed upon cleaving. However, the dangling bonds of the phosphorous surface atoms are unstable. Therefore, these P surface atoms can be evaporated or removed by the high-energy photons in beamlines and hence reform the surface to the next-termination plane which is more stable. In the end, the surface possibly becomes P6 terminated over a relatively short period of time

In order to resolve the different experimental results, we have theoretically investigated several other (001) surface terminations and find that the calculated Fermi surface of the P7-terminated (001) surface, shown in Fig. 5(c), is in

good agreement with experiment (see Supplemental Material for more detail [48]). Figure 5(b) shows the calculated stripelike Fermi surface consisting of nontrivial surface states surrounding the bulk pocket, which move away from the center as the energy is lowered from the Fermi level to 500 meV below it. Note that the zigzag-shaped P7-terminated surface which is composed solely of phosphorous atoms in Fig. 4(c) exhibits a larger degree of roughness compared to the P6-terminated surface [Fig. 3(c)] (see Supplemental Material for unrotated data [48]). Due to this surface environment, the energy dispersion of surface states varies across Fermi level and can be easily observed in regions where bulk states are gapped out [see Fig. 5(d)]. These nontrivial surface states emerge from the crossing point between the Γ and \overline{X} points [indicated by a yellow arrow in Fig. 5(d)] which is projected from the PT symmetry protected nodal loop away from the yz plane in Fig. 1(c) (see Supplemental Material for discussion on SOC effect [48]). These surface states are difficult to resolve on the P6-terminated surface [Fig. 3(d)]. The calculations reveal how the surface conditions and terminations affect the sensitivity of the energy dispersion of topologically nontrivial surface states.

IV. CONCLUSION

In conclusion, we perform a systematic study of HfP_2 using ARPES and first-principles calculations. Our theoretical study leads to the discovery of nontrivial surface states that exist as a result of topological nodal lines in our system. Our experimental data show surface states predicted by calculations and support the discovery of nontrivial topology in the nodal-line semimetal HfP_2 . While the bulk states remain largely unaffected, the surface termination of cleaved HfP_2 plays a crucial role in the resulting nontrivial band structure

of the (001) surface. The ARPES results show that the Fermi surface in an aged (fresh) sample matches with the calculation of the P6-terminated (P7-terminated) (001) surface. Since the surface with P6 termination [Fig. 3(d)] likely has higher formation energy than the P7 termination [Fig. 5(d)], it is plausible that a cleaved surface could gradually degrade from P7 to P6 termination. Our results provide evidence that surface termination or local environment plays an important role in the surface electronic structure of HfP₂.

ACKNOWLEDGMENTS

M.N. is supported by U.S. AFOSR Grant No. FA9550-17-1-0415 and NSF CAREER Grant No. DMR-1847962. C.S. is supported by the American Physical Society Bridge Program as well as MPS Alliances for Graduate Education and the Professoriate Graduate Research Supplements. The work at California State University, Northridge was supported

by NSF Partnership for Research and Education in Materials Grant No. DMR-1828019. H.L. acknowledges the support by the Ministry of Science and Technology (MOST) in Taiwan under grant number MOST 109-2112-M-001-014-MY3. T.-R.C. was supported by the Young Scholar Fellowship Program from the Ministry of Science and Technology (MOST) in Taiwan, under a MOST grant for the Columbus Program MOST108-2636- M-006-002, National Cheng Kung University, Taiwan, and National Center for Theoretical Sciences, Taiwan. This work was supported partially by the MOST, Taiwan, Grant MOST107-2627-E-006-001. This research was supported in part by Higher Education Sprout Project, Ministry of Education to the Headquarters of University Advancement at National Cheng Kung University (NCKU). This research used resources of the Advanced Light Source, a U.S. Department of Energy Office of Science User Facility, under Contract No. DE-AC02-05CH11231. We thank Sung-Kwan Mo for beamline assistance at Lawrence Berkeley National Lab (LBNL).

- [1] M. Z. Hasan and C. L. Kane, Rev. Mod. Phys. 82, 3045 (2010).
- [2] X.-L. Qi and S.-C. Zhang, Rev. Mod. Phys. 83, 1057 (2011).
- [3] A. Bansil, H. Lin, and T. Das, Rev. Mod. Phys. 88, 021004 (2016).
- [4] N. P. Armitage, E. J. Mele, and A. Vishwanath, Rev. Mod. Phys. 90, 015001 (2018).
- [5] L. Fu, C. L. Kane, and E. J. Mele, Phys. Rev. Lett. 98, 106803 (2007).
- [6] Y. Xia, D. Qian, D. Hsieh, L. Wray, A. Pal, H. Lin, A. Bansil, D. Grauer, Y. S. Hor, R. J. Cava, and M. Z. Hasan, Nat. Phys. 5, 398 (2009).
- [7] T. H. Hsieh, H. Lin, J. Liu, W. Duan, A. Bansil, and L. Fu, Nat. Commun. 3, 982 (2012).
- [8] S.-M. Huang, S.-Y. Xu, I. Belopolski, C.-C. Lee, G. Chang, B. Wang, N. Alidoust, G. Bian, M. Neupane, C. Zhang, S. Jia, A. Bansil, H. Lin, and M. Z. Hasan, Nat. Commun. 6, 7373 (2015).
- [9] H. Weng, C. Fang, Z. Fang, B. A. Bernevig, and X. Dai, Phys. Rev. X 5, 011029 (2015).
- [10] S.-Y. Xu, I. Belopolski, N. Alidoust, M. Neupane, G. Bian, C. Zhang, R. Sankar, G. Chang, Z. Yuan, C.-C. Lee, S.-M. Huang, H. Zheng, J. Ma, D. S. Sanchez, B. Wang, A. Bansil, F. Chou, P. P. Shibayev, H. Lin, S. Jia, and M. Z. Hasan, Science 349, 613 (2015).
- [11] B. Q. Lv, H. M. Weng, B. B. Fu, X. P. Wang, H. Miao, J. Ma, P. Richard, X. C. Huang, L. X. Zhao, G. F. Chen, Z. Fang, X. Dai, T. Qian, and H. Ding, Phys. Rev. X 5, 031013 (2015).
- [12] Z. Wang, H. Weng, Q. Wu, X. Dai, and Z. Fang, Phys. Rev. B 88, 125427 (2013).
- [13] M. Neupane, S.-Y. Xu, R. Sankar, N. Alidoust, G. Bian, C. Liu, I. Belopolski, T.-R. Chang, H.-T. Jeng, H. Lin, A. Bansil, F. Chou, and M. Z. Hasan, Nat. Commun. 5, 3786 (2014).
- [14] A. A. Burkov, M. D. Hook, and L. Balents, Phys. Rev. B 84, 235126 (2011).
- [15] G. Bian, T.-R. Chang, R. Sankar, S.-Y. Xu, H. Zheng, T. Neupert, C.-K. Chiu, S.-M. Huang, G. Chang, I. Belopolski, D. S. Sanchez, M. Neupane, N. Alidoust, C. Liu, B. Wang, C.-C.

- Lee, H.-T. Jeng, C. Zhang, Z. Yuan, S. Jia, A. Bansil, F. Chou, H. Lin, and M. Z. Hasan, Nat. Commun. 7, 10556 (2016).
- [16] L. M. Schoop, M. N. Ali, C. Straßer, A. Topp, A. Varykhalov, D. Marchenko, V. Duppel, S. S. P. Parkin, B. V. Lotsch, and C. R. Ast, Nat. Commun. 7, 11696 (2016).
- [17] M. Neupane, I. Belopolski, M. M. Hosen, D. S. Sanchez, R. Sankar, M. Szlawska, S.-Y. Xu, K. Dimitri, N. Dhakal, P. Maldonado, P. M. Oppeneer, D. Kaczorowski, F. Chou, M. Z. Hasan, and T. Durakiewicz, Phys. Rev. B 93, 201104(R) (2016).
- [18] M. M. Hosen, K. Dimitri, I. Belopolski, P. Maldonado, R. Sankar, N. Dhakal, G. Dhakal, T. Cole, P. M. Oppeneer, D. Kaczorowski, F. Chou, M. Z. Hasan, T. Durakiewicz, and M. Neupane, Phys. Rev. B 95, 161101(R) (2017).
- [19] M. M. Hosen, K. Dimitri, A. K. Nandy, A. Aperis, R. Sankar, G. Dhakal, P. Maldonado, F. Kabir, C. Sims, F. Chou, D. Kaczorowski, T. Durakiewicz, P. M. Oppeneer, and M. Neupane, Nat. Commun. 9, 3002 (2018).
- [20] C.-K. Chiu and A. P. Schnyder, Phys. Rev. B 90, 205136 (2014).
- [21] S.-Y. Yang, H. Yang, E. Derunova, S. S. P. Parkin, B. Yan, and M. N. Ali, Adv. Phys. X 3, 1414631 (2018).
- [22] C. Fang, M. J. Gilbert, X. Dai, and B. A. Bernevig, Phys. Rev. Lett. 108, 266802 (2012).
- [23] B. Bradlyn, J. Cano, Z. Wang, M. G. Vergniory, C. Felser, R. J. Cava, and B. A. Bernevig, Science 353, aaf5037 (2016).
- [24] G. Autès, D. Gresch, M. Troyer, A. A. Soluyanov, and O. V. Yazyev, Phys. Rev. Lett. 117, 066402 (2016).
- [25] S. Li, Y. Liu, S.-S. Wang, Z.-M. Yu, S. Guan, X.-L. Sheng, Y. Yao, and S. A. Yang, Phys. Rev. B 97, 045131 (2018).
- [26] K. Wang, D. Graf, L. Li, L. Wang, and C. Petrovic, Sci. Rep. 4, 7328 (2014).
- [27] C. Xu, J. Chen, G.-X. Zhi, Y. Li, J. Dai, and C. Cao, Phys. Rev. B 93, 195106 (2016).
- [28] Z. Yuan, H. Lu, Y. Liu, J. Wang, and S. Jia, Phys. Rev. B 93, 184405 (2016).
- [29] B. Shen, X. Deng, G. Kotliar, and N. Ni, Phys. Rev. B 93, 195119 (2016).

- [30] Y. Luo, R. D. McDonald, P. F. S. Rosa, B. Scott, N. Wakeham, N. J. Ghimire, E. D. Bauer, J. D. Thompson, and F. Ronning, Sci. Rep. 6, 27294 (2016).
- [31] Y.-Y. Wang, Q.-H. Yu, P.-J. Guo, K. Liu, and T.-L. Xia, Phys. Rev. B **94**, 041103(R) (2016).
- [32] Y. Li, L. Li, J. Wang, T. Wang, X. Xu, C. Xi, C. Cao, and J. Dai, Phys. Rev. B 94, 121115(R) (2016).
- [33] Y. Li, C. An, C. Hua, X. Chen, Y. Zhou, Y. Zhou, R. Zhang, C. Park, Z. Wang, Y. Lu, Y. Zheng, Z. Yang, and Z.-A. Xu, npj Quantum Mater. 3, 58 (2018).
- [34] A. Pariari, R. Singha, S. Roy, B. Satpati, and P. Mandal, Sci. Rep. 8, 10527 (2018).
- [35] Y. Zhou, C. Gu, X. Chen, Y. Zhou, C. An, and Z. Yang, J. Solid State Chem. 265, 359 (2018).
- [36] K.-W. Chen, S. Das, D. Rhodes, S. Memaran, T. Besara, T. Siegrist, E. Manousakis, L. Balicas, and R. E. Baumbach, J. Phys.: Condens. Matter 28, 14LT01 (2016).
- [37] N. Kumar, Y. Sun, N. Xu, K. Manna, M. Yao, V. Süss, I. Leermakers, O. Young, T. Förster, M. Schmidt, H. Borrmann, B. Yan, U. Zeitler, M. Shi, C. Felser, and C. Shekhar, Nat. Commun. 8, 1642 (2017).
- [38] L.-L. Sun, Y.-Y. Wang, S. Xu, and T.-L. Xia, Europhys. Lett. **120**, 37002 (2017).

- [39] J. Du, Z. Lou, S. N. Zhang, Y. Zhou, B. Xu, Q. Chen, Y. Tang, S. Chen, H. Chen, Q. Zhu, H. Wang, J. Yang, Q. S. Wu, O. V. Yazyev, and M. Fang, Phys. Rev. B 97, 245101 (2018).
- [40] F. Hulliger, Nature **204**, 775 (1964).
- [41] G. Kresse and J. Hafner, Phys. Rev. B 48, 13115 (1993).
- [42] J. P. Perdew, K. Burke, and M. Ernzerhof, Phys. Rev. Lett. 77, 3865 (1996).
- [43] A. A. Mostofi, J. R. Yates, G. Pizzi, Y.-S. Lee, I. Souza, D. Vanderbilt, and N. Marzari, Comput. Phys. Commun. 185, 2309 (2014).
- [44] M. P. L. Sancho, J. M. L. Sancho, J. M. L. Sancho, and J. Rubio, J. Phys. F 15, 851 (1985).
- [45] Q. Wu, S. Zhang, H.-F. Song, M. Troyer, and A. A. Soluyanov, Comput. Phys. Commun. 224, 405 (2018).
- [46] R. Yu, X. L. Qi, A. Bernevig, Z. Fang, and X. Dai, Phys. Rev. B 84, 075119 (2011).
- [47] C. Fang, Y. Chen, H.-Y. Kee, and L. Fu, Phys. Rev. B 92, 081201(R) (2015)
- [48] See Supplemental Material at http://link.aps.org/supplemental/ 10.1103/PhysRevMaterials.4.054201 for a description of surface terminations, photon energy dependent measurements, and second derivative data.